Use of Electron Diffraction and High-Resolution Imaging To Explain Why the Non-dipolar 1,3,5-Triamino-2,4,6-trinitrobenzene Displays Strong Powder Second Harmonic Generation Efficiency

Ingrid G. Voigt-Martin,*,† Gao Li,† Alexander A. Yakimanski,†,§ J. Jens Wolff,‡ and Hans Gross||

Institut für Physikalische Chemie der Johannes-Gutenberg-Universität Mainz, Jacob-Welder-Weg 11, D-55099 Mainz, Germany, the Organisch-Chemisches Institut der Ruprecht-Karls-Universität Heidelberg, Im Neuenheimer Feld 270, D-69120 Heidelberg, Germany, and Institut für Zellbiologie, E. T. H Zürich, Hönggerberg, CH-8093 Zürich, Switzerland

Received: January 13, 1997; In Final Form: April 19, 1997[⊗]

The structure of 1,3,5-triamino-2,4,6-trinitrobenzene (TATB) has been reinvestigated by a combination of electron diffraction, high-resolution imaging, simulations of electron diffraction patterns and images, and packing energy calculations. A new model is proposed that is capable of explaining the large second harmonic generation effect observed in TATB crystalline powder.

1. Introduction

The exploration of light for applications in optical integrated devices (e.g. frequency conversion, optical parametric amplification and oscillation, electrooptic modulation) has received intensive world-wide attention during the past decade.[1] Organic compounds are of interest because of their large hyperpolarizabilities and fast response times. They also allow for many different processing geometries such as thin films or fibers. The optimization of properties, however, requires an intimate understanding of the molecular architecture and conformation, the relationship between molecular orientations and crystal axes in the crystalline phase (structure) and their effect on physical properties.

In order to achieve high molecular second-order polarizabilities, β, previous concepts have relied on the combination of an electron-donating group and an electron-accepting group, linked together by a suitable conjugated π-system. There exists a wealth of literature regarding the second harmonic generation (SHG) efficiency of organic molecules and its measurement by EFISH experiments.[2] These measurements are performed in solution, and since they depend on the alignment of dipoles, they require that the molecule has a permanent dipole moment, μ. It is the projection of the vectorial part of β in the direction of μ that is measured. This can lead to apparent discrepancies with hyper Rayleigh scattering (HRS) measurements[3,4] where different tensor components of β are measured. As shown by PM3 calculations,[4] discrepancies in the data for 4-(dimethylamino)-3-cyanobiphenyl arose because the vector part of β was dominated by a single component which was roughly perpendicular to the dipole. Consequently, although the value of β as measured by EFISH was virtually zero, there was a sizeable value as measured by HRS. Detailed structure analysis of the crystals by electron diffraction showed that while the eight molecules per unit cell do not adopt a centrosymmetric structure in the solid state, their mutual arrangement led to only two relatively weak tensorial components that contributed to the observed macroscopic second-order susceptibility $\chi^{(2)}$ in the crystal. In such systems, which can be described by a two-state model, the second-order polarizability β within the dipolar approximation is proportional to $\Delta\mu$, the difference between the dipole moments in the ground state and the first allowed singlet charge transfer excited state.[5]

In contrast to this, Zyss has presented detailed calculations concerning the appearance of a quadratic optical susceptibility in molecules where symmetry in the individual molecules leads to complete cancellation of all dipole moments, in both the excited and ground states.[6] The origin of the NLO effect in such molecules is then an octopolar contribution to β and $\chi^{(2)}$, while the vectorial components are cancelled. For non-centrosymmetric arrangements of molecules in a unit cell the individual components of the quadratic susceptibility tensor can be calculated for various space groups.[7] When such molecules crystallize in a centrosymmetric arrangement, there is a mutual cancellation of all tensor components including the off-diagonal ones, and therefore there is no SHG.

The relationship between β_{ijk} with molecular coordinates i, j, k and the macroscopic optical susceptibility $\chi^{(2)}$ in macroscopic coordinates I, J, K is[1]

$$\chi^{(2)}_{IJK}(-\omega;\omega_1,\omega_2) = \frac{N}{V} f_I(\omega)\, f_J(\omega_1)\, f_K(\omega_2) \times \sum_s \sum_{ijk} \cos\theta^{(s)}_{Ii} \cos\theta^{(s)}_{Jj} \cos\theta^{(s)}_{kk}\, \beta_{ijk}(-\omega,\omega_1,\omega_2)$$

where V is the unit cell volume, N is the number of molecules per unit cell, $f_I(\omega)$ are local field factors at the frequency ω for the I-direction in the crystal, and the θ_{Ii} are the rotation angles relating microscopic and macroscopic axes. The local field factors $f_I(\omega)$ depend on the linear polarizabiliby term α_{II}, which is related to the refractive indices of the crystal. The macroscopic susceptibility coefficients d_{IJK} which are actually measured in an experiment are related to the direction of the incoming and outgoing beams with respect to the crystal axes and depend on the crystal symmetry.[1]

The investigations to be presented here concern such an "octopolar" molecule 1,3,5-triamino-2,4,6-trinitrobenzene (TATB).

* To whom all correspondence should be addressed.
† Institut für Physikalische Chemie der Johannes-Gutenberg-Universität Mainz.
§ Permanent address: Institute of Macromolecular Compounds, Bolshoi pr. 31, 199004 St. Petersburg, Russia.
‡ Organisch-Chemisches Institut der Ruprecht-Karls-Universität Heidelberg.
|| Institut für Zellbiologie, E.T.H. Zürich.
⊗ Abstract published in *Advance ACS Abstracts,* August 1, 1997.

S1089-5639(97)00193-X CCC: $14.00

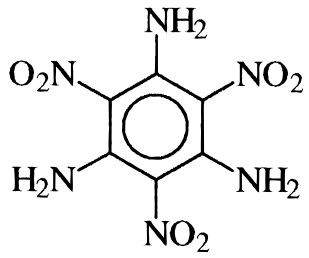

Figure 1. Molecular structure of 1,3,5-triamino-2,4,6-trinitrobenzene.

The molecular geometry is shown in Figure 1. For such molecules β has no dipolar contribution $\beta_{J=1}$ but only an octopolar one $\beta_{J=3}$:[6]

$$\beta = \beta_{J=1} \oplus \beta_{J=3} = \beta_{J=3}$$

and

$$|\beta|^2 = |\beta_{J=1}|^2 + |\beta_{J=3}|^2 = |\beta_{J=3}|^2$$

For planar trigonal molecules such as TATB with D_{3h} symmetry[6,7]

$$\beta = \beta_{J=3} = \beta_{xxx} \cdot X \cdot (X^2 - 3Y^2) + \beta_{yyy} \cdot Y \cdot (Y^2 - 3X^2)$$

using the Zyss notation in which X^3 stands for the symmetric tensor product of basis set elements $e_x \oplus e_x \oplus e_x$, etc.

Therefore, the appearance of a strong SHG signal from this non-dipolar molecule is now understood. The problem that arises with the crystals of these molecules is that although they have been determined by X-ray analysis as being centrosymmetric $P\bar{1}$, $Z = 2$, $a = 9.01$ Å, $b = 9.03$ Å, $c = 6.81$ Å, $\alpha = 108.6°$, $\beta = 91.82°$, $\gamma = 119.97°$,[9] TATB powder consisting of microcrystals shows very strong SHG.[10] Gavezzotti has suggested as possible explanations that there may be small $P1$ domains in the $P\bar{1}$ structure and that torsional librations of the nitro groups around the C−N bond by about 12° are possible.[11] Lattice defects have also been suggested as a possible reason.

Since TATB and its alkylated derivatives have aroused considerable interest[8,10−14] as a paradigmatic representative of non-dipolar molecules with high second-order polarizabilities, we have been motivated to re-examine its crystal structure using a combination of electron diffraction analysis and high-resolution imaging.

2. Experimental Methods

2.1. Optical Measurement on Crystals. Crystals were screened for SHG response by irradiating them with infrared light (wavelength $\lambda = 1064$ nm) using the fundamental beam of a Q-switched Nd:YLF laser. The incident beam (TEM beam diameter 0.9 mm, polarization 100:1) is focused by a beam-splitting mirror onto the sample placed on a microscope specimen stage.[15] The fundamental intensity in the plane of the crystal would be 10^8 V/cm^2, so an infrared filter is positioned in front of the objective lens to protect the sample. If the sample generates a second-harmonic signal, an additional bandpass filter ($\lambda = 532.5$ nm) guarantees that only this signal reaches the detector.

2.2. Sample Preparation for Structure Analysis. TATB was dissolved in hot DMSO (150 °C) at a concentration of 0.1% (wt %). A drop of the TATB solution was placed on carbon-coated mica. When the solvent was evaporated, the carbon film with TATB crystals on it was transferred onto a water surface and then the floating carbon film was picked up with an electron microscope grid.

TATB crystals were very thin (about 100 Å) with lateral dimensions of about 2 μm × 2 μm. This is sufficiently large for electron diffraction analysis. There is only one paper in which a successful X-ray structure analysis is reported for this sample,[9] because it is extremely difficult to obtain sufficiently large single crystals.

2.3. Electron Diffraction. The samples placed on electron microscopic grids as described in section 2.2 were investigated in a Philips EM-300 electron microscope with a eucentric goniometer stage. The individual crystals can be rotated and

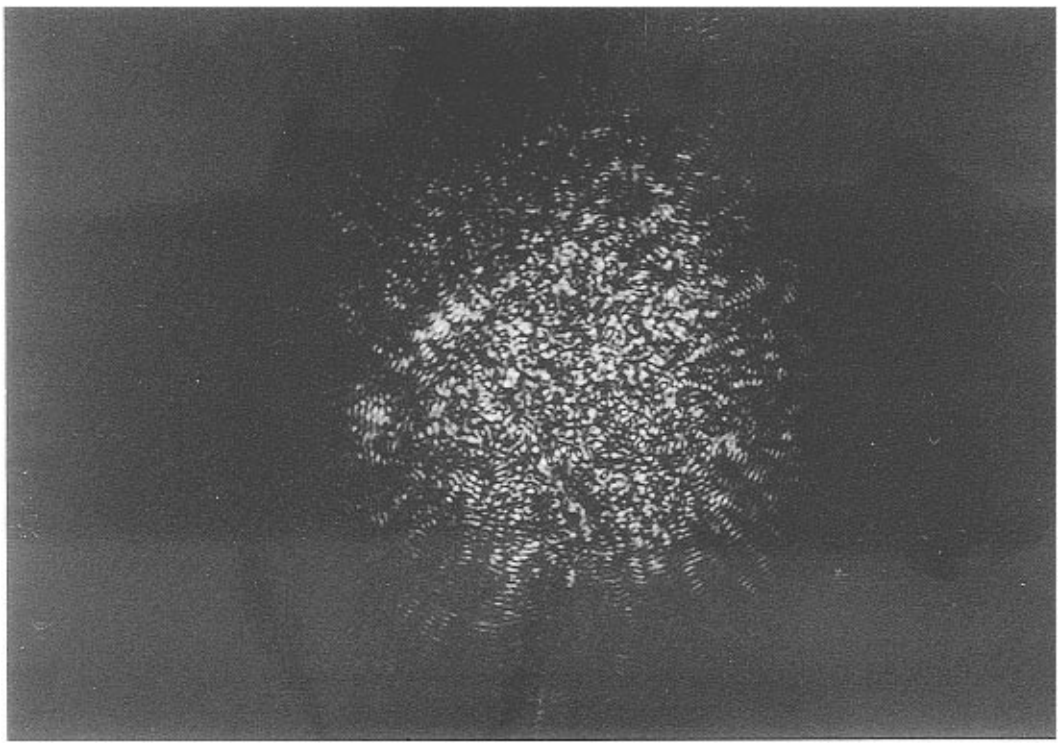

Figure 2. SHG signal from TATB crystalline powder.

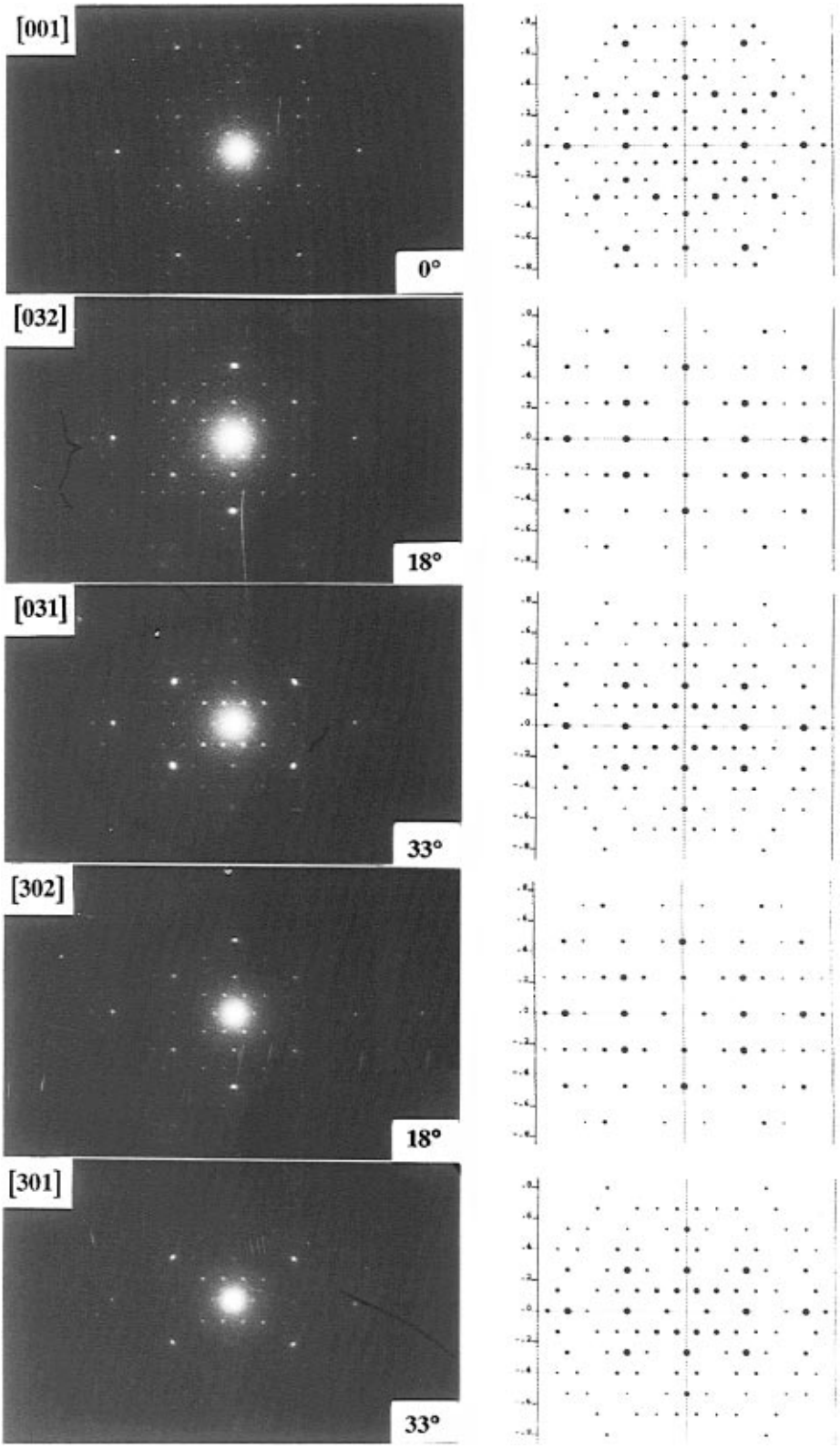

Figure 3. Experimental and simulated electron diffraction patterns for the tilting along the (100) axis.

tilted up to ±60°. Details of the experimental procedure have been published in several papers.[16−19] A short resume is given below.

(1) The basic zone is established by tilting about significant axes and determining the positions corresponding to the largest *d*-spacing.

(2) An axis with strong reflections is established and chosen as the tilt axis. The diffraction pattern first disappears and reappears when a new zonal projection is reached, the angle is noted, and the process is repeated. The tilting is always performed both to the right and to the left direction.

(3) A second axis is chosen as the tilt axis (if possible perpendicular to the first one) and the procedure repeated.

From these experiments the unit cell dimensions can be determined. On the basis of observed extinctions, it is generally possible to reduce the number of possible space groups to two or three. During subsequent molecular modeling, the possible number of space groups can normally be further reduced.

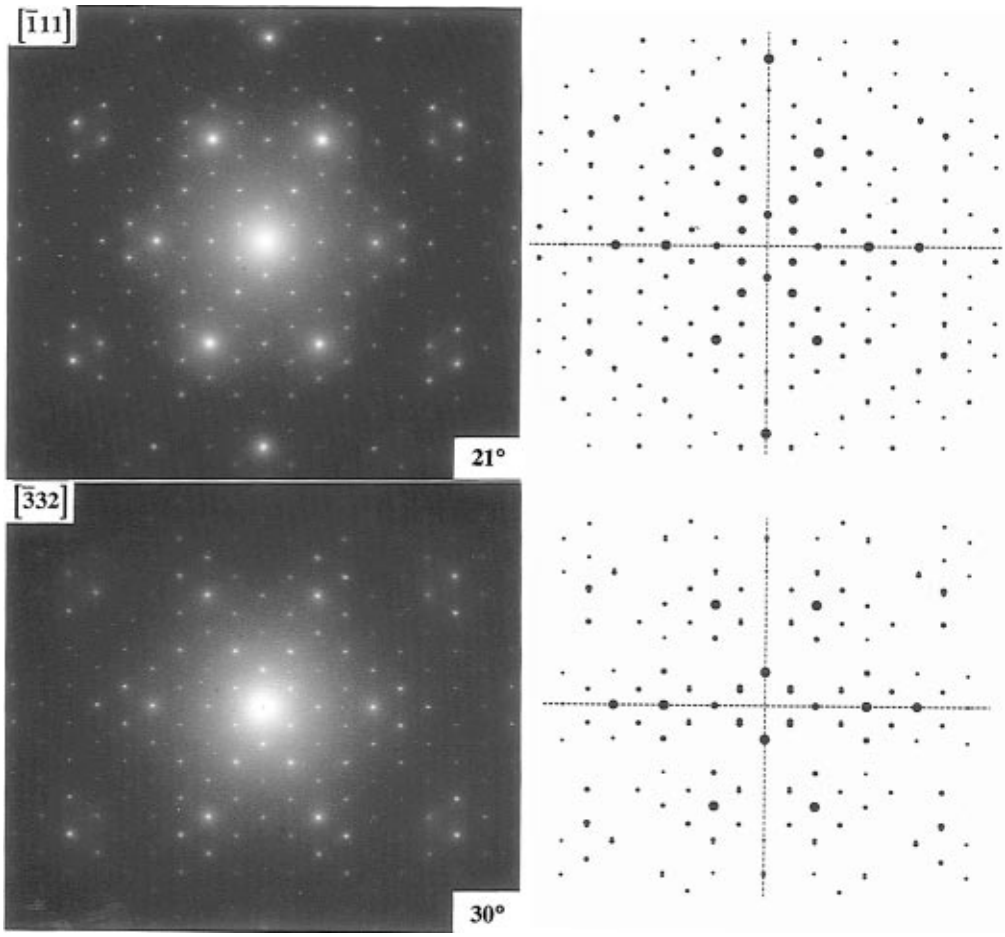

Figure 4. Experimental and simulated electron diffraction patterns for the tilting along the (110) axis.

2.4. High Resolution Electron Microscopy. High-resolution images were obtained with a Gatan slow scan CCD Model 694 attached to a Philips CM 12. Imaging organic samples is best achieved by previously adjusting the phase contrast function for transfer of the required spatial frequencies on an adjacent area of the sample as described previously.[16−19] The use of an electron microscope with a digital output enabling precise control of the lens currents greatly facilitates the procedure. Although lattice planes cannot always be directly reviewed on the monitor, a fast Fourier transform of the image enables a quick decision to be made regarding the suitability of the area in question for imaging and whether the correct transfer function has been chosen. Speed is essential to prevent degradation of a sample in the electron beam.

2.5. Powder X-ray Diffraction. X-ray powder diffraction patterns were obtained by standard methods using a Siemens D500 diffractometer (Cu Kα radiation with a wavelength of 1.542 Å) in a $\theta/2\theta$ X-ray reflectivity mode. Since the number of reflections does not suffice for Rietveld methods, structure determination is not possible. However, with the aid of the electron diffraction patterns, consistent indexing can be achieved and the cell parameters not available in the tilting experiments can usually be derived.

3. Computational Methods

3.1. Generation of the Molecular Model. The minimum energy gas phase conformations of the molecule were calculated by semiempirical quantum mechanical methods incorporated in MOPAC. The method has been established in quantum chemistry for many years.[20] The PM3 method incorporated in the program package MOPAC 6.0 was used, which is optimized for reproducing such molecular properties as heats of formation and dipole moments. Most molecules produce several minimum energy conformations. To begin the simulation, the conformation that can be best fitted into the experimentally determined unit cell is chosen. For this conformation the dipole moment, the linear polarizability, and the hyperpolarizability tensors are calculated in the molecular coordinate system.

3.2. Simulation of Electron Diffraction Patterns Using Calculated Crystal Structures. The prediction of crystal structures from a knowledge of molecular architecture was initiated by Kitaigorodsky.[21] In recent years considerable effort has been expended in attempts to predict crystal structures from a knowledge of the molecular architecture.[22−25] Attempts to calculate the potential energy hypersurface of organic crystals have not been at all unsuccessful. Gavezzotti uses the 6-exp empirical potential:[26]

$$E = A\exp(-Br) - Cr^{-6}$$

for organic crystals containing C, H, N, O, Cl, and S. Computational simplification is achieved using the atom−atom approximation.[27] A vast amount of information on packing modes is available through thousands of crystal structures collected in the Cambridge Database. Therefore, simple and effective potentials have become available such as the (1) Dreiding force field;[28] (2) PCK method;[29] and (3) cluster method,[22] in which clusters consisting of two to four molecules are built, by application of the most common symmetry elements (inversion center, screw axis, glide plane). The relative importance of these elements, as well as lattice translation, in building the cohesive energy of the crystal is assessed by means of a statistical analysis of known hydrocarbon structures.

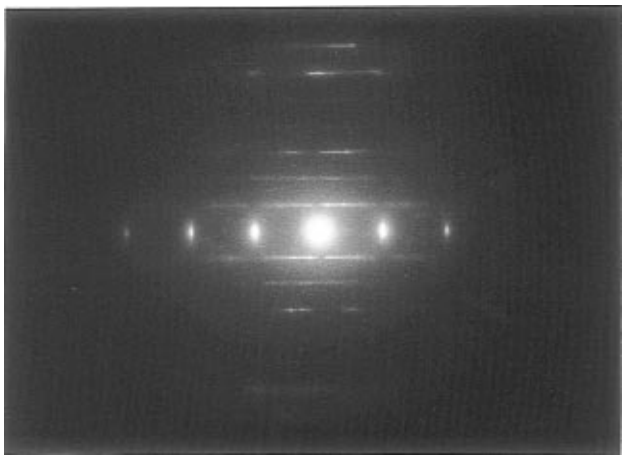

Figure 5. Electron diffraction pattern obtained from TATB crystal fragment, indicating the [100] zone.

With all of these methods it has usually been possible to locate several local minima with similar negative packing energies which differ by only a few kcal/mol, but it is difficult to assess which of these structures will occur in practice. This is a consequence of the conformational polymorphism prevalent in organic crystals because complex equilibria between polymorphic forms are already established in solution and interconversions between them are frequent.[30] Consequently, crystallization is extremely sensitive to experimental conditions.

In this work, we have chosen to calculate the packing energy of the crystals using CERIUS software distributed by Molecular Simulations. The calculated crystal structures with negative packing energies must conform to the symmetry group found by electron diffraction. In addition, the diffraction patterns calculated from the hypothetical structure must conform to the experimental ones in all projections and give rise to a reasonable *R*-value.

The simulation of the electron diffraction patterns requires the experimental determination of the unit cell parameters and the space group. The molecule in the computed geometry is placed into the unit cell using the molecular modeling program CERIUS such that the symmetry requirements based on the experimentally observed extinctions are satisfied. In addition, the number of molecules per unit cell must produce the experimentally estimated density value.

Initially, the packing energy is generally positive and a number of nonallowed close contacts are observed. These can be eliminated by adjustment of both translation and rotation of suitable subunits. Subsequently the crystal-packing energy is again minimized until a negative value is obtained. Its value is determined by a superposition of various two-center, three-center, and four-center bonded and nonbonded interactions:

$$E = E_{vdw} + E_{coul} + E_{hb} + E_{tor}$$

(a) The nonbonded van der Waals term (E_{vdw}) is generally treated using the Lennard-Jones 6−12 potential form, $E_{vdw} = Ar^{-12} - Br^{-6}$ but the exp(−6) form can also be chosen:[26] $E_{vdw} = Ae^{-Cr} - Br^{-6}$, where *A*, *B*, and *C* are empirical parameters and *r* is the interatomic distance.

(b) The Ewald summation technique is used to calculate the Coulomb energy: $E_{coul} = 322.0637\sum_{i>j}(Q_iQ_j/\epsilon r_{ij})$, where the constant effects the conversion to kcal/mol, ϵ is the dielectric constant, and $Q_{i,j}$ are atomic charges. We used here the Q_i values for the planar TATB molecule in the gas phase, calculated by the PM3 method[20] implemented into the MOPAC 6.0 program package. The calculated values of atomic charges are quite large (e.g., −0.70, 1.36, −0.64*e* on C, N, O atoms of $C-NO_2$ fragments, respectively). Therefore, TATB crystals differ from ordinary organic crystals for which the Coulombic contribution to the total energy is usually negligibly small.[21] It is well-known that for strongly ionic crystals a reliable calculation of E_{coul} is a difficult problem because of the divergency of lattice summation series.[31] The Ewald summation method employed in the CERIUS program package can produce large errors in these cases. Therefore, the calculated E_{coul} values presented in the following discussion may only be considered as rather approximate.

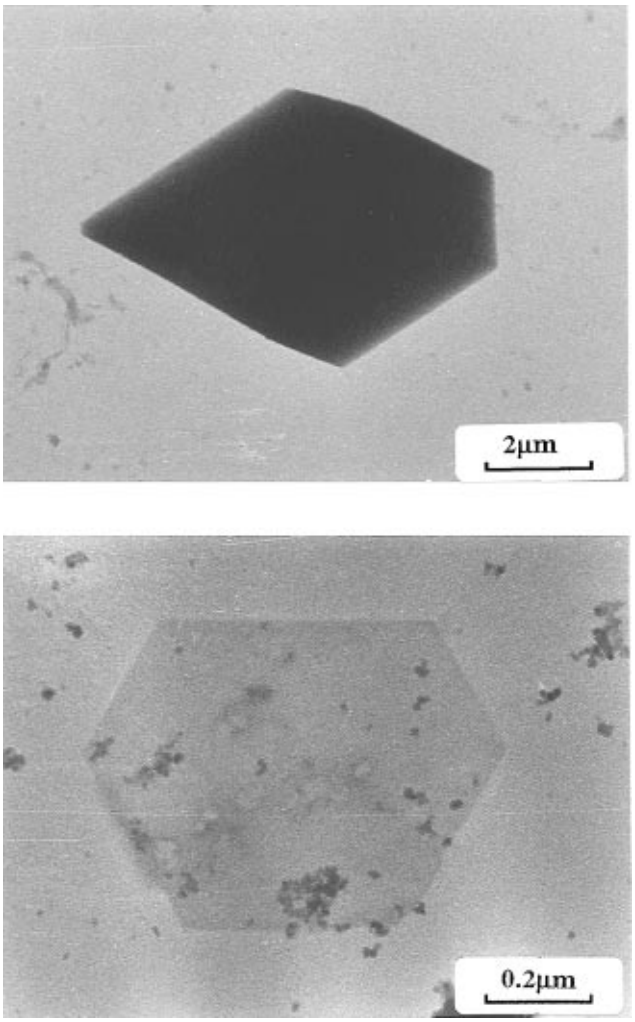

Figure 6. Two different observed morphologies of TATB crystals: (a, top) thick crystal, corresponding to the structure reported in literature; (b, bottom) thin crystal, corresponding to the simulated structure.

(c) The energy of the hydrogen bonds (E_{hb}) is calculated using a CHARM-like potential: $E_{hb} = D_{hb}[5(r_{hb}/r_{DA})^{12} - 6(r_{hb}/r_{DA})^{10}]\cos^4(\theta_{DHA})$. θ_{DHA} is the bond angle hydrogen donor (D)−hydrogen−hydrogen acceptor (A), while r_{DA} is the distance between the donor and acceptor. There is an enormous amount of statistical material about hydrogen bond patterns in the Cambridge Database.

(d) A Dreiding force field is used for the calculation of subrotation torsional interactions E_{tor}. However, it is important to note that we optimize the molecular valence geometry (bond lengths and bond angles) previously by semiempirical quantum mechanical calculations. It is well-known that the changes in molecular geometry during crystallization generally involve only the subrotations. Consequently, the Dreiding force field is used only to optimize a known gas phase conformation in the crystal.

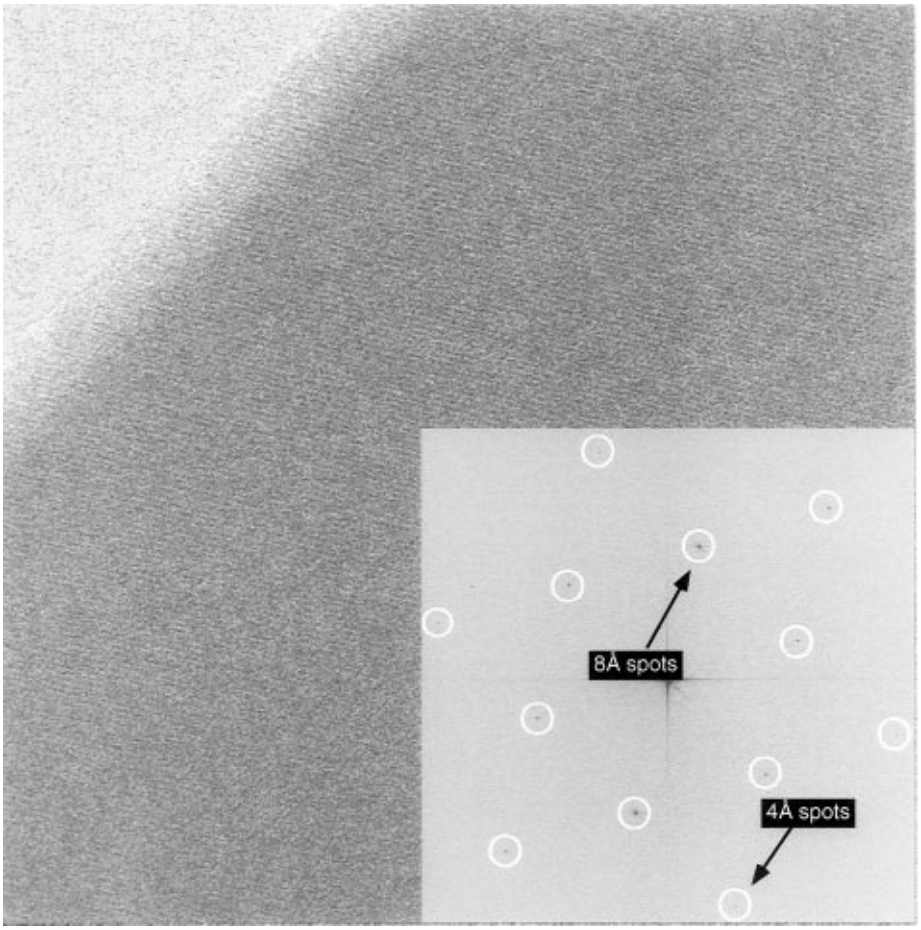

Figure 7. High-resolution image of TATB and Fourier transform (bottom right-hand corner) from the *ab*-plane of TATB thin crystals.

The parameters involved in these expressions are well-known for the molecules and bonds in question and have been continuously updated during the past decade.

The symmetry and packing restrictions imposed by the experimental electron diffraction patterns and the need to simulate these in many different zones have enabled us to solve several unknown structures.[4,16−19] Indeed, in some cases it has been possible to quantify the electron diffraction intensity values and calculate the structure using maximum entropy and log-likelihood statistics. In each case the simulated structure was confirmed.

The values of different components of α, μ, β are calculated for the modified molecular conformation in the crystal state, initially in molecular coordinates *i, j, k* and then in those related to crystallographic coordinates *I, J, K* by applying a suitable rotation matrix and using crystal symmetry conditions.[1] When the structure is solved, the molecular coordinates can also be related directly to the unit cell axes *a, b, c*.

4. Results

4.1. Optical Measurements. A drop of solution containing microcrystals was put on a microscope slide, and the solution was allowed to evaporate. The illuminating infrared laser beam was excluded by a suitable filter and the crystals in transmission gave a strong green signal, indicating that second-harmonic generation had taken place (Figure 2).

4.2. Electron Diffraction. The experimental electron diffraction patterns obtained in the tilting experiment are shown on the left-hand side of Figures 3 and 4. The tilting angles (bottom right-hand corner) are indicated, and the tilting axis is (100). Tilting to the right and to the left gave identical diffraction patterns. The [001] zone has the appearance of a star of David. In the interstices of the star, the sixth-order reflections are very strong. However, the reflections surrounding this maximum do not have hexagonal symmetry. It is also noteworthy that during the tilting experiments we did not obtain the normal distinguishable succession of diffraction zones usually observed in organic crystals with a short *c*-axis, but instead, a continuous series of electron diffraction patterns, which made it very difficult to distinguish one zone from the subsequent one. This observation immediately indicates a long *c*-axis. Tilting about the (110) direction (Figure 4) revealed the [$\bar{1}$11] and [$\bar{3}$32] zones at 21° and 30°. Tilting about the *a*-axis (Figure 3) revealed the [032] and [031] zones at 18° and 33°, respectively. Tilting about the *b*-axis (Figure 3) revealed the [302] and [301] zones at 18° and 33°. Tilting to the right and to the left gives rise to a continuous series of diffraction patterns which are identical in opposite tilt directions.

These observations indicate that the *c*-axis is long and that the *ab*-plane is perpendicular to it. All diffraction patterns have very characteristic and reproducible features: (1) very strong (300), (320), (030) reflections; (2) very strong (600) and symmetry-related reflections; (3) characteristic nonhexagonal distribution of intensities around (600) and symmetrically related reflections.

A noteworthy diffraction pattern is shown in Figure 5, which was obtained from a crystalline fragment. Here the strong reflections at the equator correspond to 3.4 Å, which is typical for the distance between aromatic rings, suggesting that the projection is either [010] or [100]. The second axis of this diffraction pattern (*a**- or *b**-axis) is perpendicular to the *c**-axis. The spacing of the first reflection on this axis corresponds to 7.8 Å (as already shown in the [001] projection).

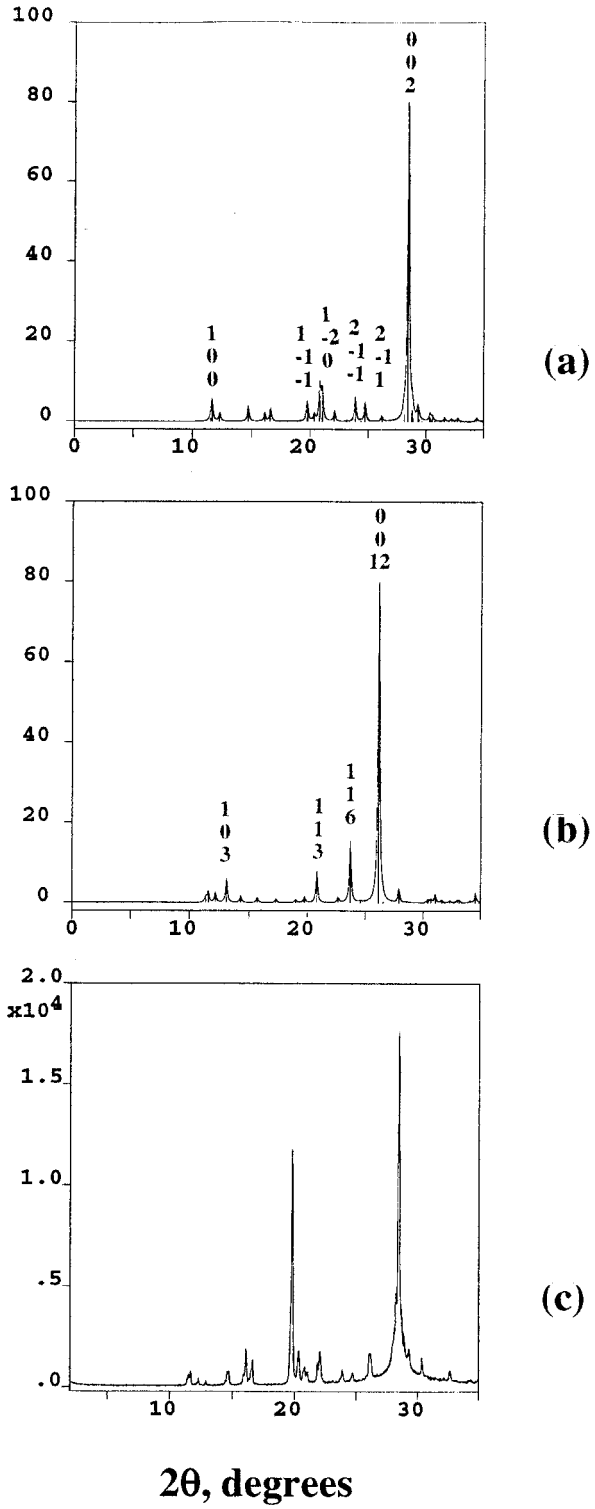

Figure 8. X-ray powder diffraction spectra for TATB: (a) simulated from the $P\bar{1}$ structure reported in literature; (b) simulated from the suggested $P3_1$ structure; (c) experimental spectrum.

Qualitatively, therefore, these diffraction patterns indicate (1) superstructures in the *a*-, *b*-, and *c*-direction; (2) that molecular symmetry in the *ab*-plane is hexagonal; and (3) that the *c*-axis is perpendicular to the *ab*-plane.

Streaking parallel to the *c**-axis indicates some disordering due to shift between layers of TATB molecules from ideal crystalline positions perpendicular to the *c*-direction. However, there are spots on the streaks, and the distance between the two strongest spots corresponds to 13.6 Å, i.e. groups consisting of four molecules. It is then obvious that three such groups give rise to a helix with a repeat period of 41 Å, and the strong reflections on the equator are (0012) reflections. Detailed analysis in the manner described previously[16−19] indicated a trigonal unit cell with the following cell constants: space group $P3_1$; $a = b = 9.00$ Å, $c = 40.90$ Å, $\gamma = 120°$.

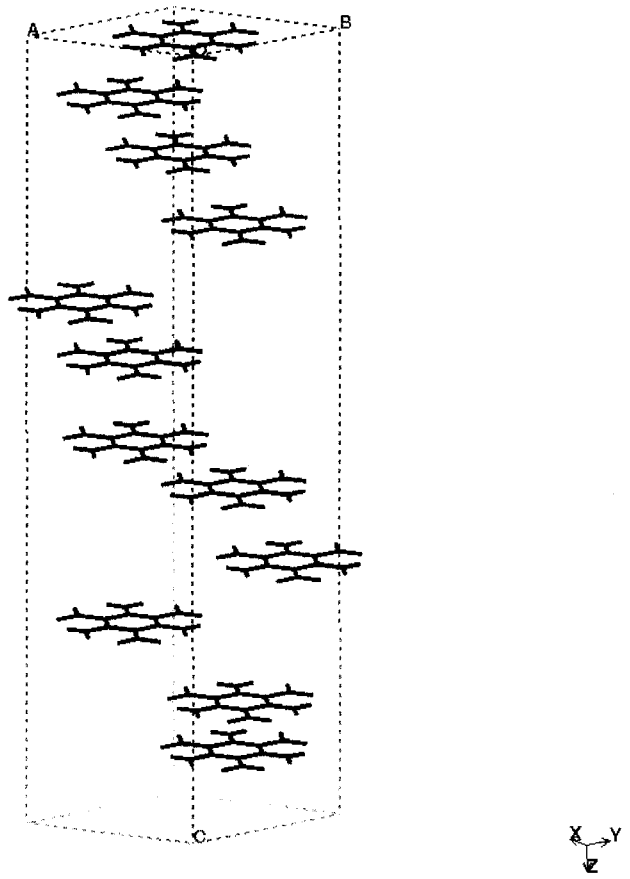

Figure 9. Simulated model with a modulated translatory wave of 12 TATB molecules per unit cell.

4.3. High-Resolution Images. Two different morphologies were observed: (a) thin, hexagonal crystals that can be penetrated by the electron beam (Figure 6b); (b) rhomboidal crystals that are too thick for examination in a transmission electron microscope (Figure 6a).

The high-resolution images of the *ab*-planes from the thin crystals are shown in Figure 7. Slight tilt makes the images appear as a series of straight lines, but careful scrutiny reveals hexagonal symmetry, as substantiated by the Fourier transform of the image (bottom right-hand corner). The crystal *ab*-planes show perfect crystalline order. There are no defects in these planes that could account for the observed second-harmonic generation.

4.4. X-ray Powder Spectrum. The experimental X-ray powder spectrum is shown in Figure 8c, together with the powder pattern calculated on the basis of the literature X-ray structure[9] (Figure 8a) and that calculated from our model (Figure 8b). The experimental powder pattern contains all the features of both calculated structures, but cannot be simulated by one of them alone. All of the peaks from the literature model agree with those from experiment, but there are additional peaks in the experimental X-ray powder diffraction diagram which can be explained by our model as (103) (absent in the X-ray powder spectrum calculated for the literature model) and (0012) peaks (intensity is very weak in the X-ray powder spectrum calculated for the literature model, but rather strong in the experimental X-ray powder diagram). Our model will be described in section

TABLE 1: Atomic Fractional Coordinates for One Independent Unit for the TATB *P*31 Crystal Structure

atom	*X*	*Y*	*Z*	atom	*X*	*Y*	*Z*	atom	*X*	*Y*	*Z*
C1	0.49332	0.33333	0.00000	N33	0.66667	0.65549	0.08333	O65	0.34109	0.20647	0.16667
C2	0.49332	0.49332	0.00000	N34	0.35583	0.33333	0.08333	O66	0.20647	0.34109	0.16667
C3	0.33333	0.49332	0.00000	N35	0.34451	0.01118	0.08333	H67	0.97933	0.08978	0.16667
C4	0.17334	0.33333	0.00000	N36	0.66667	0.02250	0.08333	H68	0.08978	0.97933	0.16667
C5	0.17335	0.17335	0.00000	O37	0.12686	0.46795	0.08333	H69	0.24355	0.55621	0.16667
C6	0.33333	0.17335	0.00000	O38	0.99224	0.19871	0.08333	H70	0.35401	0.77712	0.16667
N7	0.65549	0.33333	0.00000	O39	0.53205	0.65891	0.08333	H71	0.77712	0.35401	0.16667
N8	0.64417	0.64417	0.00000	O40	0.80129	0.79353	0.08333	H72	0.55621	0.24355	0.16667
N9	0.33333	0.65549	0.00000	O41	0.34109	−0.12686	0.08333	C73	0.49332	0.66667	0.25000
N10	0.02250	0.33333	0.00000	O42	0.20647	0.00776	0.08333	C74	0.49332	0.82665	0.25000
N11	0.01118	0.01118	0.00000	H43	0.97933	0.75645	0.08333	C75	0.3333	0.82665	0.25000
N12	0.33333	0.02250	0.00000	H44	0.08978	0.64599	0.08333	C76	0.17335	0.66667	0.25000
O13	0.79353	0.46795	0.00000	H45	0.24355	0.22288	0.08333	C77	0.17335	0.50668	0.25000
O14	0.65891	0.19871	0.00000	H46	0.35401	0.44379	0.08333	C78	0.33333	0.50668	0.25000
O15	0.19871	0.65891	0.00000	H47	0.77712	0.02067	0.08333	N79	0.65549	0.66667	0.25000
O16	0.46795	0.79353	0.00000	H48	0.55621	−0.08978	0.08333	N80	0.64417	0.97750	0.25000
O17	0.00776	−0.12686	0.00000	C49	0.82665	0.666667	0.16667	N81	0.33333	0.98882	0.25000
O18	−0.12686	0.00776	0.00000	C50	0.82665	0.82665	0.16667	N82	0.02250	0.66667	0.25000
H19	0.64599	0.75645	0.00000	C51	0.66667	0.82665	0.16667	N83	0.01118	0.34451	0.25000
H20	0.75645	0.64599	0.00000	C52	0.50668	0.66667	0.16667	N84	0.33333	0.35583	0.25000
H21	−0.08978	0.22288	0.00000	C53	0.50668	0.50668	0.16667	O85	0.79353	0.80129	0.25000
H22	0.02067	0.44379	0.00000	C54	0.66667	0.50668	0.16667	O86	0.65891	0.53205	0.25000
H23	0.44379	0.02067	0.00000	N55	0.98882	0.66667	0.16667	O87	0.19871	0.99224	0.25000
H24	0.22288	−0.08978	0.00000	N56	0.97750	0.97750	0.16667	O88	0.46795	0.12686	0.25000
C25	0.82665	0.33333	0.08333	N57	0.66667	0.98882	0.16667	O89	0.00776	0.20647	0.25000
C26	0.82665	0.49332	0.08333	N58	0.35583	0.66667	0.16667	O90	−0.12686	0.34109	0.25000
C27	0.66667	0.49332	0.08333	N59	0.34451	0.34451	0.16667	H91	0.64599	0.08978	0.25000
C28	0.50668	0.33333	0.08333	N60	0.66667	0.35583	0.16667	H92	0.75645	0.97933	0.25000
C29	0.50668	0.17335	0.08333	O61	0.12686	0.80129	0.16667	H93	−0.08978	0.55621	0.25000
C30	0.66667	0.17335	0.08333	O62	0.99224	0.53205	0.16667	H94	0.02067	0.77712	0.25000
N31	0.98882	0.33333	0.08333	O63	0.53205	0.99224	0.16667	H95	0.44379	0.35401	0.25000
N32	0.97750	0.64417	0.08333	O64	0.80129	0.12686	0.16667	H96	0.22288	0.24355	0.25000

4.6. It appears, therefore, that the powder sample is polymorphic and contains both types of crystals.

4.5. Molecular Model. The PM3 method was used for the geometry optimization of the TATB molecule. Three different possible structures were found with planar D_{3h}, chair-like C_{3v}, and boat-like C_s geometries and calculated heats of formation of −9.6, −10.3, and −10.5 kcal/mol, respectively. It appeared that the best agreement between the simulated and experimental electron diffraction patterns was achieved with the planar TATB molecular structure, although, according to the PM-3 results, this structure is not the most stable in the gas phase.[32a] However, the difference in stability between the D_{3h} and the most stable C_s structure is only ca. 1 kcal/mol. Therefore, the results obtained from the simulation procedure should indicate which is the correct conformation.

4.6. Simulation of Diffraction Patterns. When modeling is initiated, the number of probable structures is already narrowed down considerably (section 4.2). The 12 molecules along the *c*-axis must be arranged in three groups of four and therefore there must be a shift between subsequent molecules. All lattice distances have now been determined. These considerations indicated a modulation on the *c*-axis. Refinement of the model led to the structure shown in Figure 9, which consists of three independent units in the unit cell, each made up of four molecules.[32b] The atomic coordinates of one independent unit are presented in Table 1.

The calculated total packing energy *E* for the structure is rather cohesive. To calculate particular *E* values for crystals with H-bonding, one may use two different options implemented into the CERIUS software: (1) to include into E_{vdw} or (2) to exclude from E_{vdw} the energies of van der Waals interactions for all hydrogen−hydrogen acceptor atom pairs forming H-bonds. These two options give different values of E_{vdw} and *E*, namely, $E_{vdw}(1)$, $E(1)$ and $E_{vdw}(2)$, $E(2)$, respectively. For the TATB crystal structure presented here, the calculated packing energies per unit cell of 12 TATB molecules are $E(1) = -297.2$ kcal/mol ($E_{vdw}(1) = -120.3$ kcal/mol, $E_{coul} = -132.7$ kcal/mol, $E_{hb} = -44.2$ kcal/mol) and $E(2) = -360.7$ kcal/mol ($E_{vdw}(2) = -183.9$ kcal/mol). The sublimation energy estimated from $E(2)$ as $-E(2)/12$ is about 30 kcal/mol.

The agreement between experimental and calculated diffraction patterns in all zones is shown in Figures 3 and 4. The *R*-factor from uncorrected intensities was calculated to be 28% (Table 2), which is a reasonable value for structure determination by electron diffraction.

Within the independent units the molecules are shifted with respect to each other as indicated. The molecules within the first independent unit have fractional coordinates (1/3,1/3,0), (2/3,1/3,1/12), (2/3,2/3,1/6), (1/3,2/3,1/4) (Table 3). The second and third independent units are produced by the $P3_1$ space group symmetry operations, leading to a translation along *c* and a subsequent rotation around the *c*-axis. The three independent units are shifted with respect to each other. In fact, this operation leads to the layered structure with a shift between any two neighboring layers by one-third of the in-plane period value ($a = b = 9$ Å), the shift being realized in one of the symmetrically equivalent directions, (100), (010), or (110) (see Table 4). The distance between the centers of the nearest molecules in every two neighboring layers is the same, but the shifting direction is different. As one can see from Figure 10 which shows a top view of the unit cell in the *ab*-projection, this shifting of neighboring layers brings nitro (amino) groups of each layer into close vicinity of amino (nitro) groups of the neighboring layers. This leads to a favorable interlayer interaction. The same effect could be achieved by a rotation of each layer with respect to its neighbors by 60° without the shift between them. However, this would result in a centrosymmetric structure, similar to that determined by X-ray analysis,[9] which would prevent the observation of $\chi^{(2)}$.

We have analyzed the possibility of a rotation of each second layer by 60° with respect to the neighboring layers in our model shown in Figures 9 and 10. However, it appeared that this rotation leads to an increase in the crystal-packing energy. Moreover, with such a model, it was not possible to simulate

TABLE 2: Comparison of the Calculated and Observed Structure Factors for *hk*0 Reflections[a]

hkl	*d*-spacing (Å)	$\|F_c\|$	$\|F_o\|$
100	7.79	22	24
010	7.79	22	25
−110	7.79	22	27
300	2.60	50	37
030	2.60	50	36
−330	2.60	50	36
600	1.30	114	88
060	1.30	114	83
−660	1.30	114	85
110	4.50	17	19
−210	4.50	17	18
−120	4.50	17	19
220	2.25	38	28
−420	2.25	38	29
−240	2.25	38	31
330	1.50	40	30
−360	1.50	40	32
−630	1.50	40	31
410	1.70	5	7
−150	1.70	5	7
−540	1.70	5	8
140	1.70	5	7
−450	1.70	5	8
−510	1.70	5	6
500	1.54	5	6
050	1.54	5	7
−550	1.54	5	9
210	2.94	10	10
−130	2.94	10	16
−320	2.94	10	13
120	2.94	10	11
−230	2.94	10	13
−310	2.94	10	14
310	2.16	7	10
−140	2.16	7	9
−430	2.16	7	8
130	2.16	7	9
−340	2.16	7	8
−410	2.16	7	9
320	1.79	9	13
−250	1.79	9	12
−530	1.79	9	12
230	1.79	9	11
−350	1.79	9	10
−520	1.79	9	12
700	1.11	34	44
070	1.11	34	48
−770	1.11	34	47
610	1.19	20	24
−170	1.19	20	25
−760	1.19	20	24
−710	1.19	20	23
160	1.19	20	26
−670	1.19	20	24
450	1.00	8	16
−590	1.00	8	15
−940	1.00	8	14
540	1.00	8	15
−490	1.00	8	14
−950	1.00	8	17

[a] $\sum|F_c| = 1314$; $\sum|F_o| = 1319$; $|F_{hkl}| = (|F_{hkl}| + |F_{-h-k-l}|)/2$; $R = 28\%$.

the correct electron diffraction patterns. This implies that the strong hydrogen bonding within molecular layers and the interaction between the layers are important structure-determining factors, a favorable interlayer interaction being achieved by a shift rather than a rotation between neighboring layers.

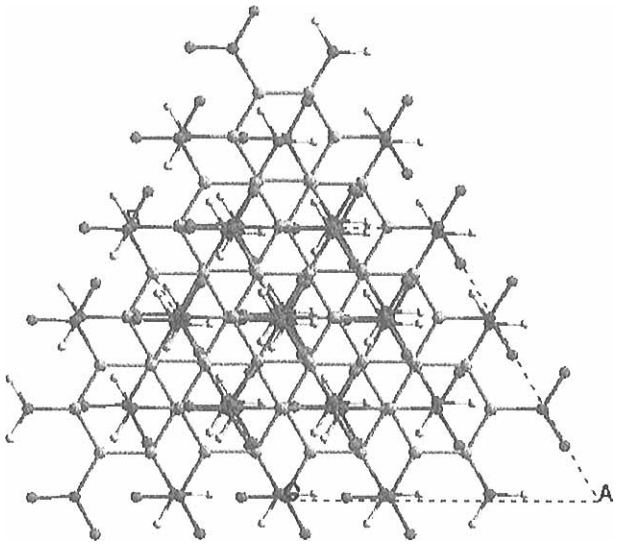

Figure 10. Top view (*ab*-projection) of the unit cell for the simulated model, indicating the close contacts between amino and nitro groups in the neighboring layers.

TABLE 3: Fractional Coordinates of Centers of TATB Molecules in the Unit Cell

molecule no.	*a*	*b*	*c*
1	1/3	1/3	0
2	2/3	1/3	1/12
3	2/3	2/3	1/6
4	1/3	2/3	1/4
5	2/3	0	1/3
6	2/3	1/3	5/12
7	1/3	0	1/2
8	1/3	2/3	7/12
9	0	2/3	2/3
10	2/3	1/3	3/4
11	0	1/3	5/6
12	1/3	2/3	11/12

TABLE 4: Relationship between the Layer *n* and the Layer *n*−1 in the Unit Cell. For Example, −(1/3)*a* + −(1/3)*b* Means That the Layer Is Shifted with Respect to the Previous Layer along −*a* and along −*b* Directions by 1/3 of *a*-Period and *b*-Period, Respectively

layer number *n*	shifted with respect to last *n*−1 layers
1 (13)	−(1/3)*b*
2	(1/3)*a*
3	(1/3)*b*
4	−(1/3)*a*
5	(1/3)*a* + (1/3)*b*
6	(1/3)*b*
7	−(1/3)*a* + −(1/3)*b*
8	−(1/3)*b*
9	−(1/3)*a*
10	−(1/3)*a* + -(1/3)*b*
11	(1/3)*a*
12	(1/3)*a* + (1/3)*b*

The model has strong and new implications for the cause of the NLO effect in TATB, as will be shown in the following section. The reasons is that the independent unit consisting of four molecules no longer has a 3-fold symmetry axis and posesses a considerable dipole moment.

4.7. Simulation of High-Resolution Images. Our model in the *ab*-projection is shown in Figure 10. The simulated images using a slice thickness of 3.4 Å and taking account of the transfer function of the 200 kV instrument are shown in Figure 11 for different sample thicknesses. They correspond to the experimental findings (hexagonal diffractogram from image) except for the strong attenuation of (100) lattice planes due to slight tilt. The simulations confirm that the superstructure

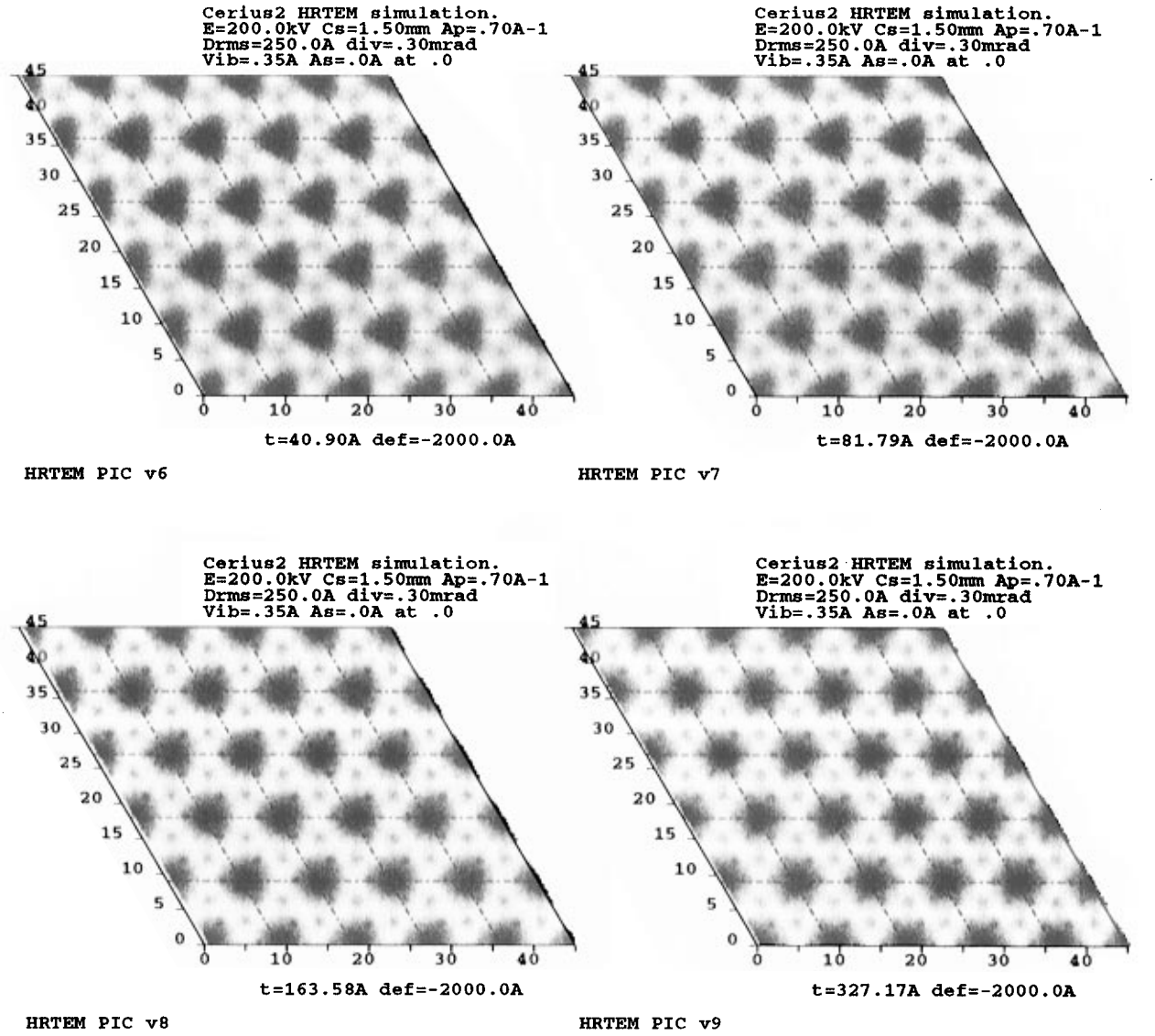

Figure 11. Simulated HREM images for different sample thicknesses.

along the *c*-axis does not destroy the hexagonal symmetry observed in the *ab*-projection.

Finally, in Figure 12, the crystal morphologies of the literature structure (Figure 12a) and our model (Figure 12b) calculated using CERIUS are presented. The agreement with the experimental morphologies (Figure 6) is very good.

4.8. Consequences of Model Structure on Optical Properties. In this section, macroscopic NLO coefficients, d_{IJK}, are estimated using the PM3 calculated values of molecular tensor components of linear polarizability α and quadratic polarizability β:

$$d_{IJK} = (N/V)f_I f_J f_K b_{IJK} = (N/V)f_I f_J f_K \sum c_{xyz}(I,J,K)\beta_{xyz} \quad (1)$$

where *I*, *J*, *K* are the crystal axes, *N* is the number of symmetrically related molecules in the unit cell of volume *V*, and b_{IJK} is the unit cell macroscopic hyperpolarizability per molecule calculated as linear combinations of the molecular hyperpolarizability tensor components β_{xyz} with the coefficients $c_{xyz}(I,J,K)$ derived for different crystal classes.[33]

Using the Lorenz−Lorentz relations

$$(n_I^2 - 1)/(n_I^2 + 2) = (4/3)\pi(N/V)\alpha_{II} \quad (2)$$

the local field factors, f_I, are

$$f_I = (n_I^2 + 2)/3 = 1/[1 - (4/3)\pi(N/V)\alpha_{II}] \quad (3)$$

where α_{II} are the diagonal components of the α-tensor of the unit cell per molecule.

Linear Optical Properties. The polarizability tensor α, calculated by the PM3 method implemented into the MOPAC package, for one independent unit consisting of four TATB molecules in the $P3_1$ unit cell and then reduced to the crystal frame *XYZ* (*Y*-axis parallel to *a*-axis, *Z*-axis parallel to the 3-fold screw *c*-axis of the crystal) has the following coefficients (in Å^3 units):

$$\alpha_{XX} = 87.3$$

$$\alpha_{XY} = 1.1; \quad \alpha_{YY} = 90.9$$

$$\alpha_{XZ} = 0.9; \quad \alpha_{YZ} = 0.5; \quad \alpha_{ZZ} = 12.5$$

The α-tensor is almost diagonal, and therefore, its diagonal values may be used for a rough estimation (in the static approximation) of the refractive indices of the crystal and the corresponding local field factors.

Using eq 3 with the number of independent units in the unit cell $N = 3$ and cell volume $V = 2865.6$ Å^3, we obtain $f_X = 1.6$; $f_Y = 1.66$; $f_Z = 1.06$.

Nonlinear Optical Properties. According to the PM3 data, the charge transfer in the independent unit of four TATB molecules is mostly realized in its *zy*-plane, β_{yyy} and β_{yzz} being the major components of the β-tensor of the independent unit. Therefore, for this independent unit the two-dimensional model,[33] relating the crystalline nonlinear tensor coefficients, b_{IJK}, to the molecular β-tensor coefficients, β_{ijk}, is valid. According to the axes convention used by Zyss and Oudar,[33] the angle α between this *zy*-plane and the 3-fold screw *Z*-axis of the crystal is $\alpha = 62.78°$.

The results of the PM3 calculations of the molecular β-tensor components necessary for the calculations within the two-dimensional model for space groups of class 3 are

$$\beta_{zzz} = -2.0 \times 10^{-30} \text{ esu}$$

$$\beta_{zyy} = 4.4 \times 10^{-30} \text{ esu}$$

$$\beta_{yyy} = -14.6 \times 10^{-30} \text{ esu}$$

$$\beta_{yzz} = 12.2 \times 10^{-30} \text{ esu}$$

This leads to the following results:

$$b_{ZZZ} = \beta_{yyy} \cos^3 \alpha = -1.4 \times 10^{-30} \text{ esu}$$

$$b_{YYY} = (1/4)(\beta_{yyy} \sin^2 \alpha - 3\beta_{yzz}) \sin \alpha = -10.7 \times 10^{-30} \text{ esu}$$

$$b_{XXX} = (1/4)(\beta_{zzz} - 3\beta_{zyy} \sin^2 \alpha) = -3.1 \times 10^{-30} \text{ esu}$$

$$b_{ZXX} = (1/2)(\beta_{yzz} + \beta_{yyy} \sin^2 \alpha) \cos \alpha = 0.2 \times 10^{-30} \text{ esu}$$

(In these equations, the β_{zzz}, β_{zyy}, β_{yzz} coefficients were used instead of β_{xxx}, β_{xyy}, β_{yxx}, respectively, as defined in ref 33, because the molecular plane of charge transfer in the independent unit is the *zy*-plane rather than the *xy*-plane, as defined in ref 33).

Thus, the major coefficient of the crystalline nonlinear tensor is b_{YYY}, which is observable in SHG experiments, according to phase-matching conditions with respect to the propagation direction.[33] The calculated d_{YYY} coefficient is

$$d_{YYY} = (N/V)(f_Y)^3 b_{YYY} = 51.4 \times 10^{-9} \text{ esu} = 21.4 \text{ pm/V}$$

This value is considerably higher than the value of $d_{XYZ} = 2.3$ pm/V obtained experimentally for urea single crystals.[34] It should be noted that semiempirical calculations by MOPAC usually underestimate considerably the components of the molecular β-tensors, especially for the molecules containing nitro groups.[35] Therefore, even accounting for the presence of the NLO-inactive $P\bar{1}$ polymorph in TATB powder, the result obtained for d_{YYY} of the $P3_1$ crystal is a reasonable explanation of the experimental observations that the powder SHG efficiency for TATB is 3−4 times higher than that of urea.[10]

The above estimations do not take into account the fact that in the TATB crystal individual molecules interact strongly with their neighbors within one layer through the H-bonds. It may be expected that the H-bonding between a nitro (amino) group of a molecule and an amino (nitro) group of a neighboring molecule causes an additional polarization of TATB molecules, leading to an enhancement of molecular nonlinearity, similarly to the H-bonding effect found in urea crystals.[36]

Using the calculated values of the components b_{XXX} and b_{YYY} of the unit cell macroscopic hyperpolarizability per molecule, it is possible to estimate the ratio ρ of the magnitude of the octopolar contribution to that of the dipolar one by the equation derived by Zyss[6] for a planar *XY*-layered structure with out-of-plane contributions to the charge transfer:

$$\rho = \{(2/3)(b^2_{XXX} + b^2_{YYY} + 6b^2_{XYY} + 6b^2_{YXX} - 3b_{XYY}b_{XXX} - 3b_{YXX}b_{YYY})/[(b_{XXX} + b_{XYY})^2 + (b_{YYY} + b_{YXX})^2]\}^{1/2} = (2/3)^{1/2}$$

Thus, the TATB $P3_1$ crystal should exhibit both dipolar and octopolar contributions to the macroscopic quadratic nonlinearity. It is important to emphasize this, because the nature of the SHG effect from a single TATB molecule is purely octopolar.[6] The difference between an isolated TATB molecule and the $P3_1$ crystal structure is that, in spite of a trigonal symmetry of the crystal structure, the independent unit in the unit cell does not have trigonal symmetry and, therefore, has a permanent dipole moment.

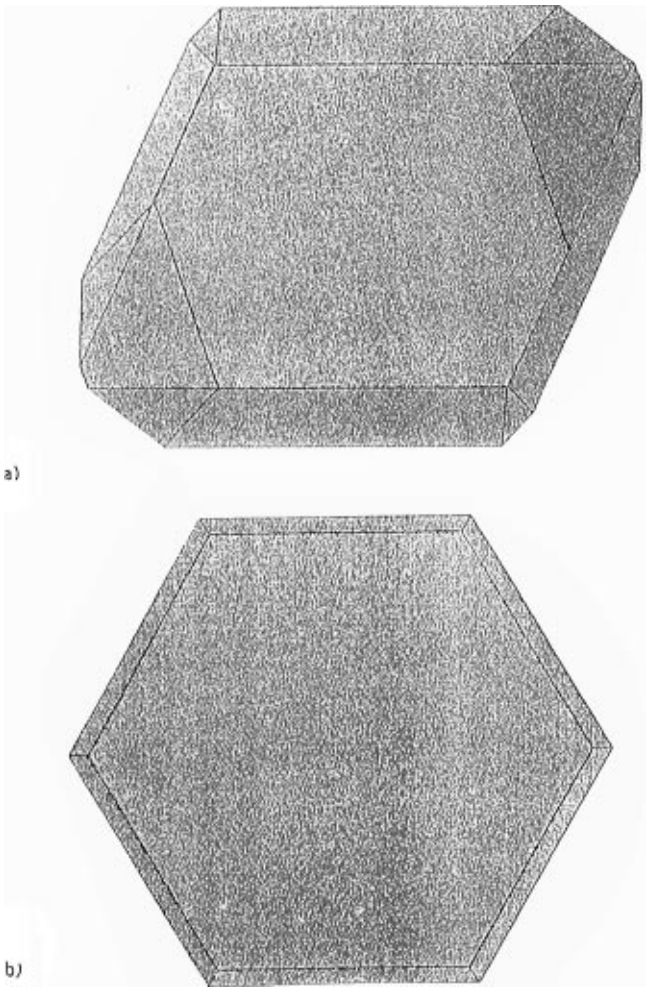

Figure 12. TATB crystal morphologies calculated using CERIUS: (a) $P\bar{1}$ crystal structure reported in literature; (b) $P3_1$ crystal structure determined by electron diffraction analysis.

5. Conclusions

The origin of second-harmonic generation in TATB has been debated for many years. There are two principal difficulties. The molecule itself is non-dipolar and the crystal structure appeared to be centrosymmetric. The former problem has been solved in a number of fundamental papers by Zyss. The latter problem has been discussed, using suggestions based on extremely probable hypotheses. In this paper, a completely new approach has been used to shed light on the crystallographic

problem, from which consequences arise for the molecular problem as well. The crystals are investigated by electron diffraction and high-resolution imaging. The results are analyzed using simulation procedures combined with packing energy calculations. Based on this combination of procedures, the following points are shown.

(1) There is polymorphism and one of the structures is centrosymmetric.

(2) There is a second type of crystal which is noncentrosymmetric and which is responsible for second-harmonic generation.

(3) On the basis of the experimental evidence it is shown that the arrangement of molecules in the unit cell is such that there are 12 molecules along the *c*-axis grouped in three independent units consisting of four molecules each.

(4) This structure is shown to have a very reasonable cohesive packing energy.

(5) The independent unit possesses a dipole moment, and therefore, there should be a dipolar contribution to the quadratic susceptibility of the crystals. In addition, there is an octopolar contribution which was shown previously to be the only one for a single TATB molecule.

(6) The individual components of the dipole moment vector, μ, and hyperpolarizability tensor per unit cell, *b*, are calculated by the PM3 method in relation to the crystal axes. The hyperpolarizability tensor component, b_{YYY}, is shown to be considerable. It is known that the calculations of molecular β-tensors based on the semiempirical quantum chemical methods are rather inaccurate, but usually represent a lower limit. The calculations, therefore, explain the observed large second harmonic generation effect.

From this combination of experimental results and theoretical considerations, the model suggested in this paper seems to be highly probable and will hopefully lead to a fruitful search for similar molecules with excellent NLO properties.

Acknowledgment. The authors are extremely grateful for financial support by the DFG in the framework of the Sonderforschungsbereich and a grant promoting German-Russian collaboration (A.Y.).

References and Notes

(1) Chemla, D. S., Zyss J., *Non-linear Optical Properties of Organic Molecules and Crystals*; Academic Press: New York, 1987.

(2) Wortmann, R.; Krämer, P.; Glania, C.; Lebus, S.; Detzer, N. *Chem. Phys.* **1993**, *173*, 99; **1994**, *229*, 101, and references therein.

(3) Wortmann, R.; Elich, K.; Lebus, S.; Liptay, W.; Borowitz, P.; Grabowska, A. *J. Phys. Chem.* **1992**, *96*, 9724.

(4) Voigt-Martin, I. G.; Zhang, Z. X.; Yan, D. H.; Yakimansky, A.; Wortmann, R. Matschiner, R.; Krämer, P.; Glania, C.; Schollmeyer, D.; Detzer, N. *Colloid Polym. Sci.* **1997**, *275*, 18.

(5) Oudar, J. L. *J. Chem. Phys.* **1977**, *67*, 446.

(6) Zyss, J.; Ledoux, I. *Chem. Rev.* **1994**, *94*, 77.

(7) Zyss, J. *Nonlinear Opt.* **1991**, *1*, 3.

(8) Baldridge, K. K.; Siegel, J. S. *J. Am. Chem. Soc.* **1993**, *115*, 10782.

(9) Cady, H. H.; Larson, A. *Acta Crystallogr.* **1965**, *18*, 495.

(10) Ledoux, I.; Zyss, J.; Siegel, J. S.; Brienne, J.; Lehn, J. M. *Chem. Phys. Lett.* **1990**, *172*, 440.

(11) Filippini, G.; Gavezzotti, A. *Chem. Phys. Lett.* **1994**, *231*, 86.

(12) (a) Maker, P. D. *Phys. Rev. A* **1970**, *1*, 923. (b) Chemla, D. S.; Oudar, J. L.; Jerphagnon, J. *Phys. Rev. B* **1975**, *12*, 4534. (c) Joffre, M.; Yaron, D.; Silbey, R. J.; Zyss, J. *J. Chem. Phys.* **1992**, *97*, 5607. (d) Zyss, J. *J. Chem. Phys.* **1993**, *98*, 6583. (e) Verbiest, T.; Clays, K.; Samyn, C.; Wolff, J. J.; Reinhoudt, D.; Persoons, A. *J. Am. Chem. Soc.* **1994**, *116*, 9320. (f) Brédas, J.-L. Meyers, F.; Pierce, B. M.; Zyss, J. *J. Am. Chem. Soc.* **1992**, *114*, 4928. (g) Brédas, J.-L.; Dehu, J.; Meyers, F.; Persoons, A.; Zyss, J. *Mol. Cryst. Liq. Cryst. Sci. Technol., Sect. B* **1994**, *6* (3−4), 263. (h) Cross, G. *Nature* **1995**, *374*, 307.

(13) Gavezzotti, A. *Acc. Chem. Res.* **1994**, *27*, 309.

(14) Wolff, J. J.; Limbach, H.-H. *Liebigs Ann. Chem.* **1991**, 691.

(15) Loos-Wildenauer, M.; Kunz, S.; Voigt-Martin, I. G.; Yakimanski, A.; Wischerhoff, E.; Zentel, R.; Tschierske, C.; Müller, M. *Adv. Mater.* **1995**, *7*, 170.

(16) Voigt-Martin, I. G.; Schumacher, M.; Garbella, R. *Macromolecules* **1992**, *25*, 961.

(17) Voigt-Martin, I. G.; Yan, D. H.; Gilmore, C.; Shankland, K.; Bricogne, G. *Ultramicroscopy* **1994**, *56*, 271.

(18) Voigt-Martin, I. G.; Simon, P.; Yan, D. H.; Yakimanski, A.; Baur, S.; Ringsdorf, H. *Macromolecules* **1995**, *28*, 243.

(19) Voigt-Martin, I. G.; Yan, D. H.; Yakimanski, A.; Schollmeyer, D.; Gilmore, C. J.; Bricogne, G. *Acta Crystallogr. Sect. A* **1995**, *51*, 849.

(20) Stewart, J. J. P. *J. Comput. Chem.* **1989**, *10*, 209.

(21) Kitaigorodski, A. *Organic Chemical Crystallography*; Consultants Bureau: New York, 1961.

(22) Gavezzotti, A.; Filippini, G. *J. Am. Chem. Soc.* **1996**, *118*, 7153.

(23) Scaringe, R. P.; Perez, S. *J. Phys. Chem.* **1987**, *91*, 2394.

(24) Williams, D. E. *Acta Crystallogr. Sect. A* **1996**, *52*, 326.

(25) Scaringe, R. P. In *Electron Crystallography of Organic Molecules*; Fryer, J.; Dorset, D., Kluwer Academic Publishers: Dordrecht, 1990.

(26) Gavezzotti, A.; Filippini, G. *J. Phys. Chem.* **1994**, *98*, 4831.

(27) Pertsin, A. J.; Kitaigorodski, A. I. *The Atom-Atom Potential Method*; Springer-Verlag: Berlin, 1987.

(28) Mayo, S. L.; Olafson, B.; Goddard, W. A., III. *J. Phys. Chem.* **1990**, *94*, 8897.

(29) Quantum Chemistry Program Exchange, Program 548, Indiana University.

(30) Gavezzotti, A. Filippini, G. *J. Am. Chem. Soc.* **1995**, *117*, 12299.

(31) Karasawa, N.; Goddard, W. A., III. *J. Phys. Chem.* **1989**, *93*, 7320.

(32) (a) PM3 is known to overestimate the amount of torsion in triaminotrinitrobenzene derivatives: Wolff, J. J.; Gredel, F.; Irngartinger, H. *Liebigs Ann. Chem.* **1996**, 1175. Ab initio calculations (HF, 6−31G*) revealed a flat hypersurface for the conformation of TATB in the gas phase; planar and nonplanar forms exist within a range of less than 1 kcal/mol: Wolff, J. J.; Frenking, G. Unpublished results. (b) Voigt-Martin, I. G.; Li, G.; Yakimanski, A.; Schulz, G.; Wolff, J. J. *J. Am. Chem. Soc.* **1996**, *118*, 12830.

(33) Zyss, J.; Oudar, J. L. *Phys. Rev.* **1982**, *A26*, 2028.

(34) Betzler, K.; Hesse, H.; Loose, P. *J. Mol. Struct.* **1978**, *47*, 393.

(35) Kurtz, H. A.; Stewart, J. J. P.; Dieter, K. M. *J. Comput. Chem.* **1990**, *11*, 82.

(36) Zyss, J. *J. Non-Cryst. Solids* **1982**, *47*, 211.